

## RCS PREDICTION FROM PLANAR NEAR-FIELD MEASUREMENTS

A. Bouzidi\* and T. Aguil

Syscom Laboratory, Engineer National School, B.P. 37, Le Belvedere 1002, Tunis, Tunisia

**Abstract**—It is well-known that, at low frequency, far-field RCS can be measured using a suitable implementation such as outdoor range or large anechoic chamber. The aim of this paper is to propose a new algorithm to predict RCS from near-field measurements. The comparison between RCS values obtained from the proposed method and those obtained from direct far-field values shows a good agreement between the two results.

### 1. INTRODUCTION

Controlling RCS is a real challenge for aeronautics and defence industry to gain important information about a system before it is built, thus saving time and resources. For these reasons, it is imperative to develop efficient techniques for RCS prediction. RCS measurement must meet with the approximate plane-wave irradiation condition. So, the target must be located at a minimal distance, the so-called far-field distance, from the illuminating and receiving antennas in order to approach such radiation condition, which needs a vast measuring area or an expansive compact range system. At high frequency, where anechoic chambers are used to simulate free-space conditions [1], probe can be placed in the far-field region of the target under test. So, the RCS is calculated directly using far-field measurements. In contrast, in the low frequency domain, it is more difficult to realize the far-field condition [2], since the dimension of anechoic chambers is generally less than the near-field/far-field boundary. In order to overcome this problem, several methods based on the concept of near-field/far-field transformation [3–7] have been proposed. The key idea behind these methods is to consider the target as an antenna under test (AUT) [8].

---

*Received 10 October 2011, Accepted 16 November 2011, Scheduled 18 November 2011*

\*Corresponding author: Afif Bouzidi (afif.bouzidi@gmail.com).

Thus, the induced current on the target's surface plays the same role as the current source of an AUT. Proceeding from this, the Fourier transformation of the measured near-field gives the far-field scattering pattern. To convert the bistatic scattering pattern into bistatic RCS a calibration procedure is required [8].

Using the angular spectrum method, we establish a relationship between the bistatic radar cross section and the two-dimensional Fourier transformation of the scattered near-field. Which allows the evaluation of the bistatic RCS from planar near-field measurements.

## 2. ANGULAR SPECTRUM METHOD

### 2.1. Basic Formalism

The angular spectrum method consists in expanding an arbitrary electromagnetic field into a series of plane waves with variable amplitudes and propagation directions. Let us consider an electric field  $\vec{E}(\vec{r})$  assumed to be known in any point  $\vec{r} = (x, y, z)$  in space, we note by  $r$  the norm of  $\vec{r}$ . By choosing an arbitrary axis  $z$ , we can define the two-dimensional Fourier transformation of  $\vec{E}(\vec{r})$  as

$$\vec{A}(k_x, k_y, z) = \frac{1}{2\pi} \int_{\mathbb{R}^2} \vec{E}(x, y, z) e^{-j(k_x x + k_y y)} dx dy \quad (1)$$

where  $\vec{r}_{||} = (x, y)$  are the Cartesian transverse coordinates and  $\vec{k}_{||} = (k_x, k_y)$  the corresponding spatial frequencies or reciprocal coordinates. Similarly, the inverse Fourier transform reads as

$$\vec{E}(x, y, z) = \frac{1}{2\pi} \int_{\mathbb{R}^2} \vec{A}(k_x, k_y, z) e^{j(k_x x + k_y y)} dk_x dk_y \quad (2)$$

In the case of a homogeneous, isotropic, linear and source-free medium, the electric field satisfies the following Helmholtz equation.

$$\nabla^2 \vec{E}(\vec{r}) + k_0^2 \vec{E}(\vec{r}) = 0 \quad (3)$$

Inserting the Equation (2) into the Equation (3) and defining

$$k_z = \sqrt{k_0^2 - (k_x^2 + k_y^2)} \quad (4)$$

We find that the Fourier spectrum  $\vec{A}$  evolves along the  $z$ -axis as

$$\vec{A}(k_x, k_y, z) = \vec{A}(k_x, k_y, 0) e^{\pm j k_z z} \quad (5)$$

The wave number  $k_z$  is then either real or imaginary and turns the factor  $e^{\pm j k_z z}$  into an oscillatory or exponentially decaying function

$$\begin{cases} k_x^2 + k_y^2 \leq k_0^2 & \text{plane waves} \\ k_x^2 + k_y^2 > k_0^2 & \text{evanescent waves} \end{cases} \quad (6)$$

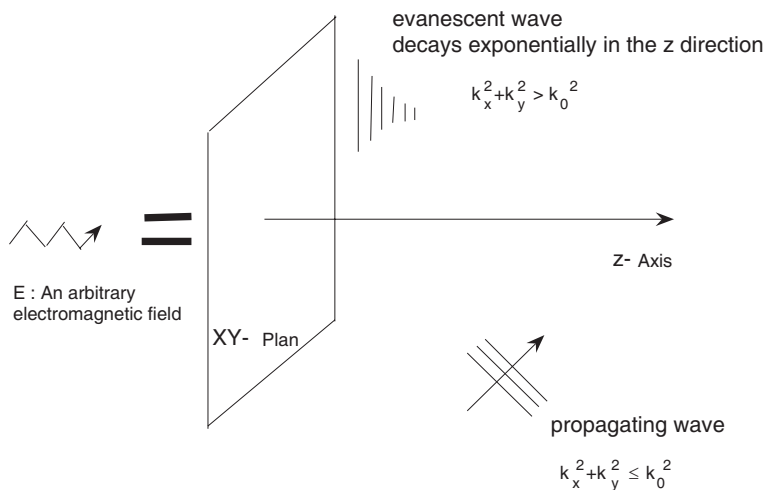


**Figure 1.** Angular spectrum representation.

So,  $\vec{E}(\vec{r})$  can be expressed as follows

$$\vec{E}(x, y, z) = \frac{1}{2\pi} \int_{\mathbb{R}^2} \vec{A}(k_x, k_y) e^{j\vec{K} \cdot \vec{r}} dk_x dk_y \tag{7}$$

where, we have set

$$\vec{K} = \vec{k}_{||} + k_z \text{sign}(z) \vec{u}_z \tag{8}$$

We find that the angular spectrum is indeed a superposition of traveling and evanescent waves as shown in Figure 1.

### 2.2. Angular Spectrum Representation of Green’s Tensor

The Green’s tensor is defined as follows

$$\vec{G}(\vec{r}) = \left( \vec{I} + \frac{1}{k_0^2} \nabla \nabla \right) G(\vec{r}) \tag{9}$$

where,  $G(\vec{r})$  is the scalar Green’s function

$$G(\vec{r}) = \frac{e^{jk_0 r}}{4\pi r} \tag{10}$$

And  $\vec{I}$  is the unit dyad.

The scalar Green’s function can be represented as two-dimensional Fourier integral

$$G(\vec{r}) = \frac{j}{2\pi} \int_{\mathbb{R}^2} \frac{e^{j(\vec{k}_{||} \cdot \vec{r}_{||} + \beta|z|)}}{4\pi\beta} d^2 k_{||} \tag{11}$$

which is commonly referred to as Weyl representation [9].

$\vec{k}_{\parallel}$  is a vector in the  $xy$ -plane and the parameter  $\beta$  is defined as

$$\beta = \begin{cases} \sqrt{k_0^2 - k_{\parallel}^2} & \text{if } k_{\parallel} < k_0 \\ j\sqrt{k_{\parallel}^2 - k_0^2} & \text{if } k_{\parallel} > k_0 \end{cases} \quad (12)$$

which shows that  $G(\vec{r})$  is written as a superposition of plane waves.

When  $k_{\parallel} < k_0$  the corresponding plane wave travels in the direction of the wave vector  $(\vec{k}_{\parallel}, \beta)$  for  $z > 0$  and  $(\vec{k}_{\parallel}, -\beta)$  for  $z < 0$  without change of amplitude.

When  $k_{\parallel} > k_0$  the wave travels in the  $xy$ -plane in the direction of  $\vec{k}_{\parallel}$ , and decays exponentially in the  $z$  direction.

The Green's tensor  $\overleftrightarrow{G}(\vec{r})$  can be represented in a similar way.

$$\overleftrightarrow{G}(\vec{r}) = \frac{1}{2\pi} \int_{\mathbb{R}^2} \frac{j}{4\pi\beta} \left( \bar{I} + \frac{1}{k_0^2} \nabla \nabla \right) e^{(j\vec{k}_{\parallel} \cdot \vec{r}_{\parallel} + j\beta|z|)} d^2k_{\parallel} \quad (13)$$

Working out the derivatives explicitly then gives the well-known result [9]

$$\overleftrightarrow{G}(\vec{r}) = \frac{1}{2\pi} \int_{\mathbb{R}^2} \frac{j}{4\pi\beta} \left( \bar{I} + \frac{1}{k_0^2} \vec{K} \vec{K} \right) e^{j\vec{K} \cdot \vec{r}} d^2k_{\parallel} \quad (14)$$

where we have set

$$\vec{K} = \vec{k}_{\parallel} + \beta \text{sign}(z) \vec{u}_z \quad (15)$$

The Equation (14) has a very transparent interpretation. Each partial wave has a wave vector  $\vec{K}$ , and it follows from Equations (12) and (15) that  $\vec{K} \cdot \vec{K} = k_0^2$ . Therefore each partial wave has the same wave number  $k_0$ , the corresponding plane wave is either traveling or evanescent, depending on the value of  $k_{\parallel}$  compared with  $k_0$  [9].

### 2.3. Angular Spectrum Representation of Scattered Field

Let consider  $\Omega$  an open subset of  $\mathbb{R}^3$  as shown in Figure 2, occupied by a homogeneous dielectric medium, and let  $\Gamma$  the boundary of  $\Omega$ .  $\varepsilon$  and  $\sigma$  denote respectively the relative electric permittivity and the conductivity of the medium.

The dielectric is illuminated by a plane linearly polarized electromagnetic wave  $(\vec{E}_i, \vec{H}_i)$

$$\vec{E}_i = E_0 e^{j\vec{K}_0 \cdot \vec{r}} \vec{p}_i \quad (16)$$

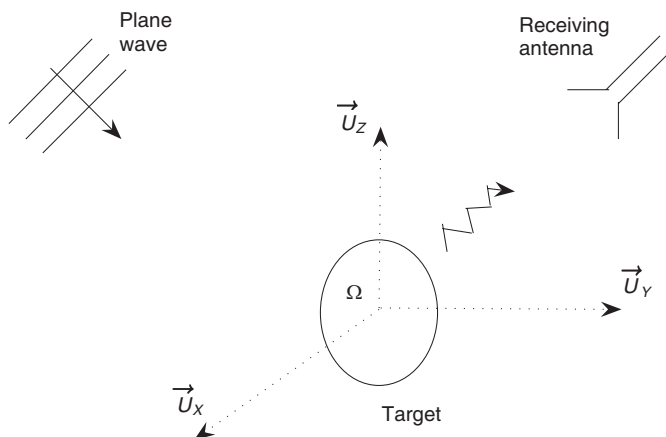


Figure 2. Scattering geometry.

$$\frac{\|\vec{E}^i\|}{\|\vec{H}^i\|} = Z_0 \tag{17}$$

where  $\vec{K}_0$ ,  $\vec{E}$ ,  $\vec{H}$  and  $\vec{p}_i$  specifying the directions of incidence, the electric field, the magnetic field and the polarization vector, respectively.

The propagation constant, permittivity and intrinsic impedance of the surrounding medium are  $k_0$ ,  $\epsilon_0$  and  $Z_0$  respectively, and a time factor  $e^{-j\omega t}$  has been assumed and suppressed.

The scattered electric field is given by [10]

$$\vec{E}^s(\vec{r}) = k_0^2 \int_{\Omega} \Delta \epsilon_r(\vec{r}') \vec{G}(\vec{r}, \vec{r}') \vec{E}(\vec{r}') dr' \tag{18}$$

where  $\vec{E}$  is the total field inside the dielectric

$$\vec{E} = \vec{E}^i + \vec{E}^s \tag{19}$$

And  $\Delta \epsilon_r(\vec{r}')$  is the difference in relative dielectric constant between the scatterer and the ambient medium.

The angular spectrum representation of  $\vec{G}(\vec{r}, \vec{r}')$  can be deduced from (14) as follows

$$\vec{G}(\vec{r}, \vec{r}') = \frac{1}{2\pi} \int_{\mathbb{R}^2} \frac{j}{4\pi\beta} \left( \vec{I} + \frac{1}{k_0^2} \vec{K} \vec{K} \right) e^{j\vec{K} \cdot (\vec{r} - \vec{r}')} d^2 k_{\parallel} \tag{20}$$

where,

$$\vec{K} = \vec{k}_{\parallel} + \beta \text{sign}(z - z') \vec{u}_z \tag{21}$$

By inserting the Equation (20) into (18), we get

$$\vec{E}^s(\vec{r}) = \frac{1}{2\pi} \int_{\Omega} \Delta \varepsilon_r(\vec{r}') \left[ \int_{\mathbb{R}^2} \frac{jk_0^2}{4\pi\beta} \left( \bar{I} + \frac{1}{k_0^2} \vec{K} \vec{K} \right) e^{j\vec{K} \cdot (\vec{r} - \vec{r}')} d^2 k_{\parallel} \right] \vec{E}(\vec{r}') dr' \quad (22)$$

It is obvious that for  $z \in ] - \infty, \min(z') \cup ] \max(z'), +\infty[$ ,  $\vec{K}$  is independent of  $z'$ .

$$\vec{K} = \vec{k}_{\parallel} + \beta \text{sign}(z - z') \vec{u}_z = \begin{cases} \vec{k}_{\parallel} - \beta \vec{u}_z, & \text{for } z \in ] - \infty, \min(z') [ \\ \vec{k}_{\parallel} + \beta \vec{u}_z, & \text{for } z \in ] \max(z'), +\infty [ \end{cases} \quad (23)$$

So, by switching the integral signs  $\int_{\mathbb{R}^2}$  and  $\int_{\Omega}$  of (22), we get

$$\vec{E}^s(\vec{r}) = \frac{1}{2\pi} \int_{\mathbb{R}^2} \frac{jk_0^2}{4\pi\beta} \left( \bar{I} + \frac{1}{k_0^2} \vec{K} \vec{K} \right) \left[ \int_{\Omega} \Delta \varepsilon_r(\vec{r}') \vec{E}(\vec{r}') e^{-j\vec{K} \cdot \vec{r}'} dr' \right] e^{j\vec{K} \cdot \vec{r}} d^2 k_{\parallel} \quad (24)$$

Finally, we deduce the angular spectrum representation of  $\vec{E}^s(\vec{r})$

$$\vec{A}^s(k_x, k_y) = \frac{jk_0^2}{4\pi\beta} \left( \bar{I} + \frac{1}{k_0^2} \vec{K} \vec{K} \right) \int_{\Omega} \Delta \varepsilon_r(\vec{r}') \vec{E}(\vec{r}') e^{-j\vec{K} \cdot \vec{r}'} dr' \quad (25)$$

$\int_{\Omega} \Delta \varepsilon_r(\vec{r}') \vec{E}(\vec{r}') e^{-j\vec{K} \cdot \vec{r}'} dr'$  represents the 3D Fourier transformation of the product  $\Delta \varepsilon_r(\vec{r}') \times \vec{E}(\vec{r}')$ . So,

$$\vec{A}^s(k_x, k_y) = \frac{jk_0^2}{4\pi\beta} \left( \bar{I} + \frac{1}{k_0^2} \vec{K} \vec{K} \right) \{ \vec{A} * H \}(k_x, k_y, \beta) \quad (26)$$

where,  $\{ \vec{A} * H \}$  is the convolution product of

$$\vec{A}(\vec{K}) = \int_{\mathbb{R}^3} \vec{E}(\vec{r}') e^{-j\vec{K} \cdot \vec{r}'} dr' \quad (27)$$

and

$$H(\vec{K}) = \int_{\Omega} \Delta \varepsilon_r(\vec{r}') e^{-j\vec{K} \cdot \vec{r}'} dr' \quad (28)$$

### 3. THE BISTATIC SCATTERING PATTERN

Assume now that distance between the target and the receiver goes to infinity. The Green's tensor is written as

$$\vec{G}(\vec{r}, \vec{r}') = \begin{pmatrix} k_0^2 G + \frac{\partial^2 G}{\partial x_1^2} & \frac{\partial^2 G}{\partial x_1 \partial x_2} & \frac{\partial^2 G}{\partial x_1 \partial x_3} \\ \frac{\partial^2 G}{\partial x_2 \partial x_3} & k_0^2 G + \frac{\partial^2 G}{\partial x_2^2} & \frac{\partial^2 G}{\partial x_2 \partial x_3} \\ \frac{\partial^2 G}{\partial x_3 \partial x_1} & \frac{\partial^2 G}{\partial x_3 \partial x_2} & k_0^2 G + \frac{\partial^2 G}{\partial x_3^2} \end{pmatrix} \quad (29)$$

where,

$$G(\vec{r}, \vec{r}') = \frac{e^{jk_0|\vec{r}-\vec{r}'|}}{4\pi|\vec{r}-\vec{r}'|} \tag{30}$$

Each element of  $\overleftrightarrow{G}(\vec{r}, \vec{r}')$  is written as  $\overleftrightarrow{G}_{im} = \delta_{im}k_0^2G + \frac{\partial^2G}{\partial x_i\partial x_m}$ ,  $(i, m) \in \{1, 2, 3\} \times \{1, 2, 3\}$

$$\delta_{im} = \begin{cases} 1 & i = m \\ 0 & i \neq m \end{cases} \tag{31}$$

We define  $R$  as,

$$R = |\vec{r} - \vec{r}'| = \left| \sum_{l=1}^3 (x_l - x'_l)^2 \right|^{\frac{1}{2}} \tag{32}$$

By applying the chain rule, we get

$$\frac{\partial^2G}{\partial x_i\partial x_m} = \frac{\partial^2G}{\partial R^2} \frac{\partial R}{\partial x_i} \frac{\partial R}{\partial x_m} + \frac{\partial G}{\partial R} \frac{\partial^2R}{\partial x_i\partial x_m} \tag{33}$$

It is easy to see that

$$\frac{\partial G}{\partial R} = \frac{jk_0R - 1}{R} \frac{e^{jk_0R}}{4\pi R} \tag{34}$$

$$\frac{\partial^2G}{\partial R^2} = (2 - 2jk_0R - k_0^2R^2) \frac{e^{jk_0R}}{4\pi R^3} \tag{35}$$

$$\frac{\partial R}{\partial x_i} = \frac{x_i - x'_i}{R} \tag{36}$$

$$\frac{\partial^2R}{\partial x_i\partial x_m} = \frac{\delta_{im}}{R} - \frac{(x_i - x'_i)(x_m - x'_m)}{R^3} \tag{37}$$

So,

$$\begin{aligned} \overleftrightarrow{G}_{im} &= (k_0^2R^2 + jk_0R - 1) \frac{G}{R^2} \delta_{im} + \\ &\frac{G}{R^2} \frac{(x_i - x'_i)(x_m - x'_m)}{R^2} (3 - 3jk_0R - k_0^2R^2) \end{aligned} \tag{38}$$

By using the far-field approximation  $k_0R \gg 1$ , the Equation (38) can be simplified as follows

$$\overleftrightarrow{G}_{im} = k_0^2G(R) \left( \delta_{im} - \frac{x_i - x'_i}{R} \frac{x_m - x'_m}{R} \right) \tag{39}$$

The Green's tensor is witted as

$$\overleftrightarrow{G} = k_0^2G(R) (I - \vec{v}\vec{v}) \tag{40}$$

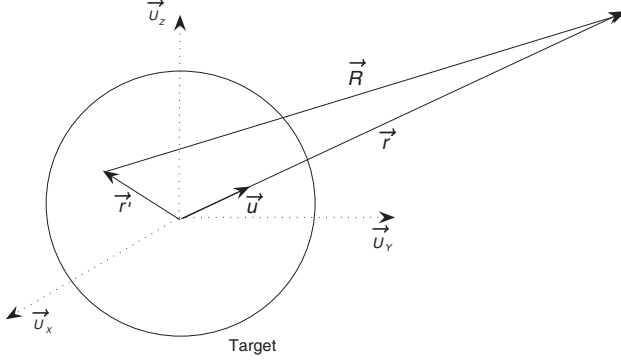


**Figure 3.** Far-field configuration.

where

$$\vec{v} = \frac{\vec{r} - \vec{r}'}{|\vec{r} - \vec{r}'|} \quad (41)$$

and

$$I = \begin{pmatrix} 1 & 0 & 0 \\ 0 & 1 & 0 \\ 0 & 0 & 1 \end{pmatrix} \quad (42)$$

The measurement point is far from the target. So,

$$R \approx r - \vec{r}' \cdot \vec{u} \quad (43)$$

$$\vec{u} = \frac{\vec{r}}{r} \quad (44)$$

$\vec{R}$  is almost parallel to  $\vec{r}$  and the only difference between them is due to the projection of  $\vec{r}'$  on  $\vec{u}$  as shown in Figure 3. In this case

$$\vec{v} \approx \vec{u} \quad (45)$$

and

$$G(R) = \frac{e^{jk_0 R}}{4\pi R} \approx \frac{e^{jk_0 r}}{4\pi r} e^{-jk_0 \vec{u} \cdot \vec{r}'} \quad (46)$$

Finally, we deduce

$$\vec{G}(\vec{r}, \vec{r}') = k_0^2 \frac{e^{jk_0 r}}{4\pi r} \left( I - \frac{1}{k_0^2} \vec{K} \vec{K} \right) e^{-j\vec{K} \cdot \vec{r}'} \quad (47)$$

where

$$\vec{K} = k_0 \vec{u} \quad (48)$$

By using the Equations (18) and (47), we deduce the scattered far-field

$$\vec{E}_{ff}^s(\vec{r}) = k_0^2 \frac{e^{jk_0 r}}{4\pi r} \left( I - \frac{1}{k_0^2} \vec{K} \vec{K} \right) \int_{\Omega} \Delta \varepsilon_r(\vec{r}') \vec{E}(\vec{r}') e^{-j\vec{K} \cdot \vec{r}'} d\vec{r}' \quad (49)$$

So,

$$\vec{E}_{ff}^s(\vec{r}) = k_0^2 \frac{e^{jk_0 r}}{4\pi r} \left( I - \frac{1}{k_0^2} \vec{K} \vec{K} \right) \{ \vec{A} * H \}(\vec{K}) \quad (50)$$

#### 4. METHODOLOGY

The RCS is defined as the surface area that intercepts the incident wave and isotropically scatters the energy. Within the far-field limit as  $r$  get large the RCS is given by the following expression

$$RCS = \lim_{r \rightarrow \infty} 4\pi r^2 \frac{\left\| \vec{E}_{ff}^s \right\|^2}{\left\| \vec{E}^i \right\|^2} \quad (51)$$

The following definitions are introduced to emphasize the polarizations of the scattered field.

$$\sigma_{\perp}^1 = \lim_{r \rightarrow \infty} 4\pi r^2 \frac{\left| \left\langle \vec{E}_{ff}^s, \vec{u}_{\perp}^1 \right\rangle \right|^2}{\left\| \vec{E}^i \right\|^2} \quad (52)$$

$$\sigma_{\perp}^2 = \lim_{r \rightarrow \infty} 4\pi r^2 \frac{\left| \left\langle \vec{E}_{ff}^s, \vec{u}_{\perp}^2 \right\rangle \right|^2}{\left\| \vec{E}^i \right\|^2} \quad (53)$$

$\langle \cdot, \cdot \rangle$  represents the dot product sign and  $(\vec{u}, \vec{u}_{\perp}^1, \vec{u}_{\perp}^2)$  is an orthonormal spherical basis.

Using the Equation (50),

$$\left\langle \vec{E}_{ff}^s, \vec{u}_{\perp}^1 \right\rangle = k_0^2 \frac{e^{jk_0 r}}{4\pi r} \left\langle \left( I - \frac{1}{k_0^2} \vec{K} \vec{K} \right) \{ \vec{A} * H \}(\vec{K}), \vec{u}_{\perp}^1 \right\rangle \quad (54)$$

It's obvious that the matrix  $\left( I - \frac{1}{k_0^2} \vec{K} \vec{K} \right)$  is real and symmetric. Hence,

$$\left\langle \vec{E}_{ff}^s, \vec{u}_{\perp}^1 \right\rangle = k_0^2 \frac{e^{jk_0 r}}{4\pi r} \left\langle \{ \vec{A} * H \}(\vec{K}), \left( I - \frac{1}{k_0^2} \vec{K} \vec{K} \right) \vec{u}_{\perp}^1 \right\rangle \quad (55)$$

We have

$$\left( I - \frac{1}{k_0^2} \vec{K} \vec{K} \right) \vec{u}_{\perp}^1 = \vec{u}_{\perp}^1 \quad (56)$$

So,

$$\left\langle \vec{E}_{ff}^s, \vec{u}_{\perp}^1 \right\rangle = k_0^2 \frac{e^{jk_0 r}}{4\pi r} \left\langle \{ \vec{A} * H \}(\vec{K}), \vec{u}_{\perp}^1 \right\rangle \quad (57)$$

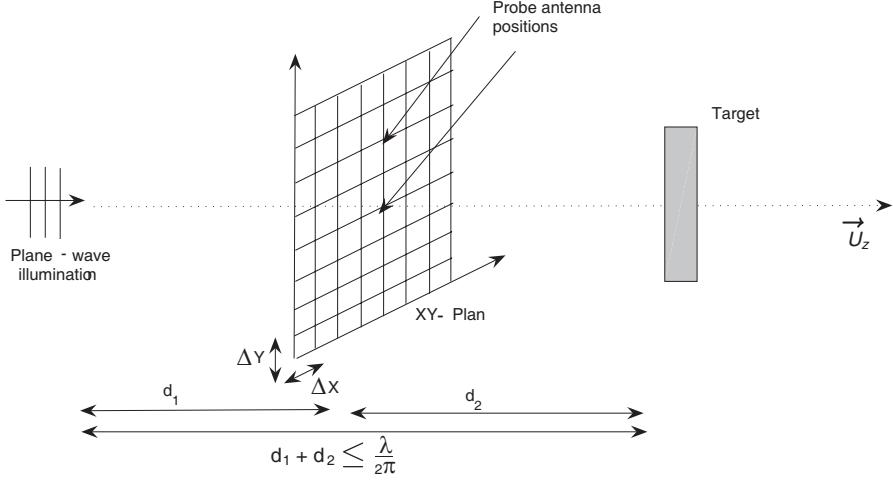


**Figure 4.** Near-field measurements.

We have from the Equation (26)

$$\langle \{\vec{A} * H\}(\vec{K}), \vec{u}_\perp^1 \rangle = -\frac{j4\pi\beta}{k_0^2} \langle \vec{A}^s, \vec{u}_\perp^1 \rangle \quad (58)$$

So,

$$\langle \vec{E}_{ff}^s, \vec{u}_\perp^1 \rangle = -j\beta \frac{e^{jk_0 r}}{r} \langle \vec{A}^s, \vec{u}_\perp^1 \rangle \quad (59)$$

Finally, we deduce

$$\sigma_\perp^1 = \frac{4\pi\beta^2}{E_0^2} \left| \langle \vec{A}^s, \vec{u}_\perp^1 \rangle \right|^2 \quad (60)$$

Similarly,

$$\sigma_\perp^2 = \frac{4\pi\beta^2}{E_0^2} \left| \langle \vec{A}^s, \vec{u}_\perp^2 \rangle \right|^2 \quad (61)$$

The relationship between the Radar cross section components and the 2D-fourier transformation of the scattered field (Equations (60) and (61)) is valid only for the traveling modes, where  $\beta$  is real. The choice of the reference  $xy$ -plane must satisfy the condition (23). The decomposition of the spherical-wave into its propagating and evanescent parts should be understood simply as a mathematical tool, that becomes meaningful only when applied to a real physical situation in which the geometry of the problem fixes the orientation of the reference plane [11–13].

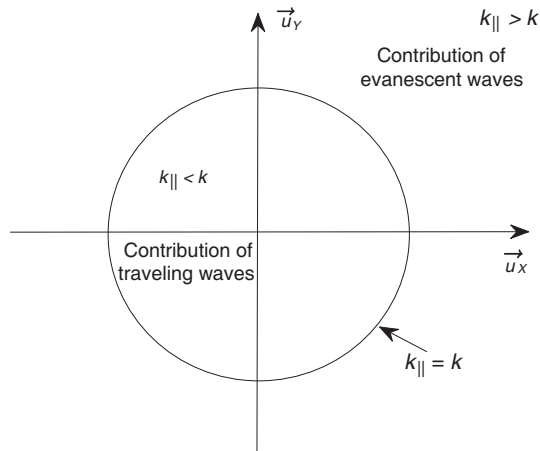


**Figure 5.** Filtering of evanescent waves.

Let us consider the following geometry configuration as shown in Figure 4.  $d$  is fixed such as  $d \leq \frac{\lambda}{2\pi}$ ,  $\frac{\lambda}{2\pi}$  represents the near-field/far-field boundary [14].

As mentioned above, the first step is determining the traveling modes of the scattered field. These modes can be deduced by filtering the planar near-field measurements by a 2D low-pass filter as shown in the Figure 5. It is well-known that, the Fourier transformation of the sampled data leads to a spectral aliasing phenomena

$$\vec{A}_{sampled}^s(k_x, k_y) = \sum_{n=-\infty}^{+\infty} \sum_{m=-\infty}^{+\infty} \vec{A}^s(k_x - \frac{n}{\Delta x}, k_y - \frac{m}{\Delta y}) \quad (62)$$

To recover  $\vec{A}^s$  from  $\vec{A}_{sampled}^s$  it is necessary to select the inner part of the rectangle

$$-\frac{\pi}{\Delta x} < k_x < \frac{\pi}{\Delta x} \quad -\frac{\pi}{\Delta y} < k_y < \frac{\pi}{\Delta y} \quad (63)$$

All traveling modes must satisfy the condition (63). So, the sampling steps  $\Delta x$  and  $\Delta y$  should verify

$$\Delta x < \frac{\lambda}{2} \quad \Delta y < \frac{\lambda}{2} \quad (64)$$

## 5. NUMERICAL EXAMPLE

In order to show the feasibility of this method, we present two numerical examples. The aim of the first one is to show the ability

of the proposed method to predict accurately the bistatic radar cross section from planar near-field measurements. The second example shows the monostatic RCS as a function of wavelength and proves the applicability of the method for a wide range of frequencies.



**Figure 6.** Missile-like object.

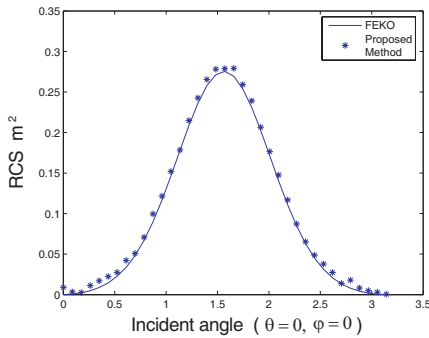


**Figure 7.** Bistatic radar cross section of a missile-like object at 100 MHz (Incident angle ( $\theta = 0$ ,  $\varphi = 0$ )).

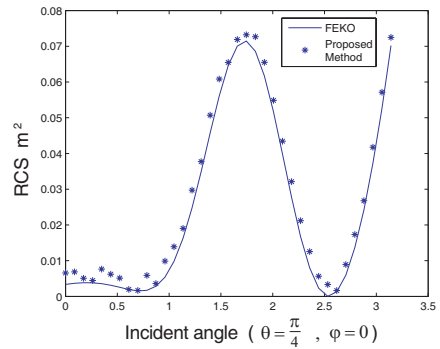


**Figure 8.** Bistatic radar cross section of a missile-like object at 100 MHz (Incident angle ( $\theta = \frac{\pi}{4}$ ,  $\varphi = 0$ )).

The Near-Field data are obtained over a planar grid using FEKO electromagnetic simulation software. In the near-field receiving configuration, the distance  $z$  between the receiving plane and the target is taken as  $z = \frac{\lambda}{4\pi}$  and the sampling space is about  $\Delta x = \Delta y = \frac{\lambda}{10}$ .

### 5.1. Bistatic Radar Cross Section of a Missile-like Object

We consider a missile-like object as shown in Figure 6 with length  $L = 2$  m, relative permittivity  $\epsilon_r = 2$  and conductivity  $\sigma = 0$ .

The target is illuminated by an incident plane wave at 100 MHz, the bistatic RCS has been studied for the incidence directions  $(\theta = \frac{\pi}{2}, \varphi = 0)$ ,  $(\theta = \frac{\pi}{4}, \varphi = 0)$  and for the scattering plane  $\varphi = 0$ . Figures 7 and 8 show a comparison between the bistatic RCS values obtained from the proposed method, and those obtained from direct far-field values using FEKO software. We observe the good agreement between both results.

### 5.2. Monostatic Radar Cross Section of a Dielectric Sphere

We consider a dielectric sphere with radius  $r = 0.5$  m, relative permittivity  $\epsilon_r = 2$  and conductivity  $\sigma = 0$ .

The illumination frequency starts from 1 MHz to 100 MHz, the mentioned interval will be divided into 100 points.

Figure 9 shows a comparison between the monostatic RCS values obtained from the proposed method, and those obtained using FEKO software.

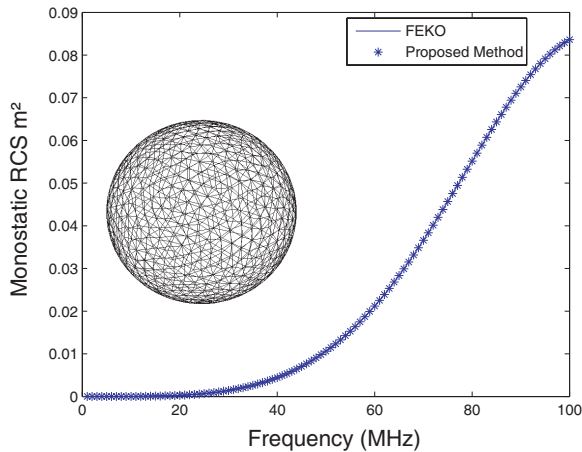


**Figure 9.** Monostatic radar cross section of a dielectric sphere frequency  $\in [1 \text{ MHz}, 100 \text{ MHz}]$ .

The established relationship between the radar cross section and the 2D-Fourier transformation of the scattered near-field is developed without any constraint related to the wavelength. So, the proposed method shows a great potential to be applied for a wide range of frequencies.

## 6. CONCLUSION

We have studied the relationship between the bistatic radar cross section and the two-dimensional Fourier transformation of the scattered near-field. Using the angular spectrum method, we showed that the scattered field can be considered as a combination of propagating and evanescent plane waves. By selecting only the propagating modes and excluding the evanescent ones in the spectrum of the measured field, we showed how to obtain bistatic RCS values from planar near-field measurements.

It should be noted that in our study, we have assumed that the target is illuminated by a plane wave. However, when it is exposed to a spherical wave, the relationship between the bistatic RCS and the 2D-Fourier transformation of the scattered near-field will need some further investigation.

## REFERENCES

1. Emerson, W. H., "Electromagnetic wave absorbers and anechoic chambers through the years," *IEEE Trans. on Antennas Propagation*, Vol. 21, No. 4, 484–490, July 1973.
2. Schluper, H. F., J. VanDamme, and V. J. Vokurka, "Optimized collimators theoretical performance limits," *AMTA Proceedings*, 313, Seattle, WA, October 1987.
3. Joy, E. B., "Basic theory of probe-compensated near-field measurements," *IEEE Trans. on Antennas Propagation*, Vol. 26, No. 3, 373–379, May 1978.
4. Wolf, E., "Three-dimensional structure determination of semi-transparent objects from holographic data," *Optics Communications*, Vol. 1, No. 4, 153–156, September/October 1969.
5. Appel-Hansen, J., "Antenna measurements," *The Handbook of Antenna Design*, Vol. 1, Ch. 8, Peter Peregrinus Ltd., London, 1982.
6. Johnson, R. C., H. A. Ecker, and J. S. Hollis, "Determination of far-field antenna patterns from near-field measurements," *Proc. IEEE*, Vol. 61, No. 12, 1668–1694, December 1973.

7. Yaghjian, A. D., "An overview of near-field antenna measurements," *IEEE Trans. on Antennas Propagation*, Vol. 34, 30–45, January 1986.
8. Leou, J. L. and H. J. Li, "Evaluation of bistatic far-field quantities from near-field measurements," *Progress In Electromagnetics Research*, Vol. 25, 167–188, 2000.
9. Arnoldus, H. F. and J. T. Foley, "Uniform asymptotic approximation of the evanescent part of the Green's tensor," *Opt. Comm.*, Vol. 207, 7–15, 2002.
10. Chew, W. C., *Waves and Fields in Inhomogeneous Media*, Van Nostrand Reinhold, New York, 1990.
11. Wolf, E. and J. T. Foley, "Do evanescent waves contribute to the far field?," *Opt. Lett.*, Vol. 23, 16–18, 1998.
12. Shchegrov, A. V. and P. S. Carney, "Far-field contribution of evanescent modes to the electromagnetic Green tensor," *J. Opt. Soc. Am. A*, Vol. 16, 2583–2584, 1999.
13. Natterer, F., *The Mathematics of Computerized Tomography*, Wiley-Teubner, 1986. Reprinted as SIAM Classics in Applied Mathematics 32, 2001.
14. Capps, C., "Near field or far field," 95–102, EDN, August 16, 2001. Available: <http://www.edn.com/contents/images/150828.pdf>. [Accessed Feb. 1, 2008].